Development of test devices for the validation of MORFEO's reconstruction and control algorithms

Edoardo Bellone de Grecis, Giulia Carlà, Lorenzo Busoni

AO4ELT7 - June 2023 - Avignon

Development of test devices for the validation of MORFEO's reconstruction and control algorithms

Edoardo Bellone de Grecis[a,b], Giulia Carlà[a], and Lorenzo Busoni[a]

[a]INAF – Arcetri Astrophysical Observatory, Largo Enrico Fermi 5, 50125, Florence, Italy
[b]Department of Physics and Astronomy - University of Florence, Via Giovanni Sansone 1, 50019, Florence, Italy

ABSTRACT

The *Multi-conjugate adaptive Optics Relay For ELT Observations* (MORFEO) shows new and challenging issues, that need to be tested and prototyped before integration and troubleshooting on sky. To do so, we aim at analyzing and testing the reconstruction and control algorithms foreseen for MORFEO through a simplified single-conjugated adaptive optics system test-bed and a numerical simulator. To inject, and also, compensate for the disturbances, we are using a 1920x1152 XY Phase Series Spatial Light Modulator manufactured by Meadowlark Optics. In this context, as a first step to our project we want to characterize it. We show the current status of the test bench and the results of the first tests.

Keywords: MCAO, Atmospheric Turbulence, MMSE Tomographic Reconstructor, PLOC, Unseen Modes, Control Algorithms, Spatial Light Modulator, SH WFS, AO Simulation

1. INTRODUCTION

The *Multi-conjugate adaptive Optics Relay For ELT Observations* (MORFEO, formerly MAORY)[1] is a post-focal adaptive optics module for the Extremely Large Telescope (ELT) [2], ESO's 40m class optical and near-infrared telescope. MORFEO is designed to support the near-infrared spectro-imager MICADO [3] and another instrument to be defined. MICADO is a first light imager instrument of the ELT working at the diffraction limit relying on the SCAO mode, available on the first light, and the MCAO mode accomplished by MORFEO. Specifically, MORFEO will provide to MICADO a diffraction limited correction over a field of view of $\simeq$1 *arcmin*, in a wide range of atmospheric conditions [4].

MORFEO has recently completed preliminary phase design [4]. It will use 12 wavefront sensors (WFS) and up to 3 deformable mirrors (DM). For the tomographic sensing, the wavefront sensors are can simultaneously

Further author information:
E.B.D.G.: E-mail: edoardo.bellone@inaf.it
G.C.: E-mail: giulia.carla@inaf.it
L.B.: E-mail: lorenzo.busoni@inaf.it

observe up to 6 Laser Guide Stars (LGS) and 3 Natural Guide Stars (NGS). Wavefront correction is performed by the ELT's adaptive M4, conjugated at 600 m, and 2 post-focal deformable mirrors, conjugated at 6 and 18 km, respectively.

MORFEO presents new and challenging issues, that need to be tested and prototyped. One of the most critical aspects of this module is the reconstruction and control algorithm.

A major limitation of multi-conjugated systems is represented by the problem of *unseen modes* [5]. This occurs when the wavefronts from different layers of the atmosphere cancel each other out. This produces a pure piston signal, to which WFSs are blind. However, from the point of view of the science camera the wavefront is not flat and therefore image quality is degraded.

To overcome the problem of *unseen modes*, MORFEO will implement a Minimum-Mean-Square-Estimator (MMSE) tomographic reconstructor [6], based on an *a priori* estimation of turbulence and noise statistics, that will be included in a Pseudo-Open Loop Control (POLC) [7]. Only few AO systems [8] used MMSE + POLC reconstructor on sky and for this reason we want to test and validate the reconstruction and control algorithm foreseen for MORFEO on a test-bench.

In this context, we aim at analyzing and testing the reconstruction and control algorithms foreseen for MORFEO through a simplified single-conjugated adaptive optics (SCAO) system test-bed and a numerical simulator. The optical setup includes a Shack-Hartmann Wavefront Sensor (SH-WFS) to sense the wavefront aberrations, a Spatial Light Modulator (SLM) to inject and also compensate for the disturbances, and a scientific camera to analyze the correction performance through the Point Spread Function (PSF). In order to simulate MORFEO's wide field, we compute the projection of the atmospheric turbulent volume along the line of sight of each WFS of MORFEO. We apply one at a time on the SLM and measure it through the SH-WFS. The measurements from each directions are used to compute the tomographic reconstruction and, consequently, to infer the commands to the SLM. The whole process is reiterated by shifting the phase maps previously simulated, in order to take into account the temporal evolution effects between successive iterations of the control loop.

In this paper, we present the preliminary phase of the project aimed to characterize a 1920x1152 XY Phase Series SLM manufactured by Meadowlark Optics. We show the current status of the test bench and the results of the first tests. Specifically, Section 2 describes the basics of Liquid Crystal On Silicon (LCoS) device for phase only modulation and how phase patterns are displayed on the SLM.

In Section 3, we provide a summary of our control and interface approach to the Spatial Light Modulator (SLM), while also highlighting the divergences from the software offered by the manufacturer.

Section 4, describes the optical scheme of the current test-bench.

In Section 5, we present the work done so far. Particularly, Section 5.1 details efforts to decrease the non-modulable spot's intensity seen in the specular reflection of the SLM. The section also covers strategies to reduce system aberration using a sensorless AO scheme in Section 5.2. Lastly, in Section 5.3, we discuss the techniques employed to deduce the SLM response to the tip/tilt displayed.

Finally, Section 6 describes the future steps and further analysis to characterize the SLM and develop the SCAO test-bench.

2. PHASE ONLY SPATIAL LIGHT MODULATOR

Reflective spatial light modulators are reflective Liquid Crystal based on Silicon (LCoS) [9] devices typically used to modulate the phase of an incident light beam by exploiting the birefringence. Liquid crystal (LC) molecules are characterised by two refractive indices along the ordinary (n_o) and extraordinary (n_e) axes. Typically, SLMs are made of nematic liquid crystal in which the molecules are aligned in an homogeneous configuration, with the direction of the extraordinary axes of the molecule defining the optical axis of the liquid crystal. A remarkable property of this material is the non-linear electro-optical response to voltage, which causes the molecules to rotate. As a result, an incoming electric field travelling in the z direction, as shown on the left of Figure 1, will experience a change in the index of refraction as a function of the applied voltage. This causes a phase delay that affects only the component of the polarisation parallel to the optical axis of the LC molecules while the orthogonal component experiences the ordinary refractive index n_0. Thus, if the incident beam is linearly polarized and

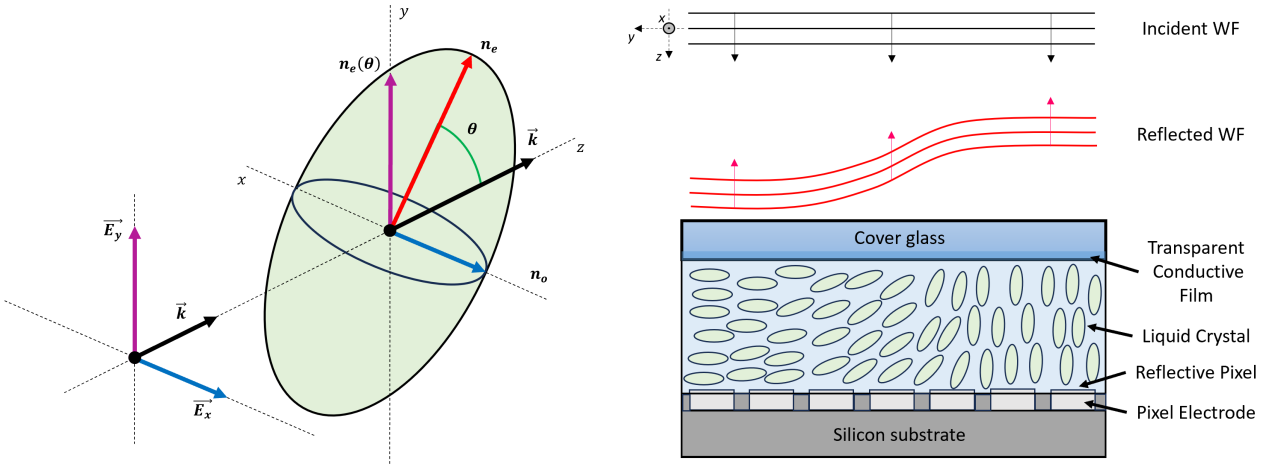

Figure 1. On the left, incidence of the unpolarised beam on the LC molecule propagating in the z-direction. The optical axis of the LC device lies on the y-axis. Due to the voltage control, the extraordinary axis n_e of the LC molecule forms an angle θ with the incident wave vector $\vec{k}$. Thus, the electric field component along the y-axis experiences an index of refraction $n_o < n_e(\theta) < n_e$. On the right is a cross-section of a reflective SLM. As the applied voltage is zero, the LC molecules are aligned to the cover glass along the y-axis, the optical axis of the LC device. This results in the maximum phase retardation of the reflected wavefront, defined by n_e. As the applied voltage increases, the molecules are oriented perpendicular to the cover glass, so that the reflected wavefront has the minimum phase delay, defined by n_o.

parallel to the extraordinary axis of the LC molecules, the outcome wavefront experiences a phase delay $\Delta\phi$ due liquid crystal molecules' orientation with respect to the wave vector $\vec{k}$ given by:

$$\Delta\phi = \frac{2\pi}{\lambda}\left(n_e(\theta) - n_o\right) 2d \tag{1}$$

where $n_e(\theta) - n_o$ is the birefringence of the LC material, θ is the angle between $\vec{k}$ and the extraordinary axis identified by the index of refraction n_e, the d is the thickness of the LC layer and λ is the wavelength.

For instance, with reference to the right panel of the Figure 1, when there is no voltage is applied to the pixel electrode, the LC molecules are aligned in a homogeneous configuration and their extraordinary axis is parallel to the SLM cover glass (in the y-direction on figure). Thus, the incident beam experiences the largest difference between the extraordinary n_e and the ordinary n_o refractive index, namely the largest phase delay. As the voltage applied to the pixel electrode increases, the LC molecules rotate until the maximum voltage is reached and they are almost perpendicular to the cover glass. In this case, the phase delay is minimal because the difference between the extraordinary and ordinary refractive indices is close to zero. [10]

Thus, when the SLM is illuminated with linearly polarized beam parallel to LC optical axis, results is a programmable phase modulator based on fixed spatial pattern, where each pixel of the SLM is independently addressable to discrete voltage values.

In this work, we use a 1920x1152 XY Phase Series SLM manufactured by Meadowlark Optics, with a resolution of 1920×1152 pixel and a pixel pitch of 9.2 μm. The SLM is calibrated by the manufacturer at $\lambda = 633$ nm to have a linear phase response to the applied voltage. Thus, phase patterns displayed on the SLM result in different phase shifts being individually addressed by each pixel, with phase shift values in the range 0-2π, represented by 256 grey levels (8-bit number, from 0 to 255).

With reference to Figure 2, the manufacturer also provides us with a Wavefront Correction (WFC) file. This is an image that is superimposed with a given phase pattern by adding the two images with a modulo 256 operation [10]. The final image is then processed by calibration. This WFC is used to remove aberrations caused by the SLM manufacturing process, which can result in a curved silicon substrate. As a result, a wavefront propagating in the liquid crystal layer experiences an additional phase delay due to the optical path associated with the non-uniform liquid crystal thickness [11].

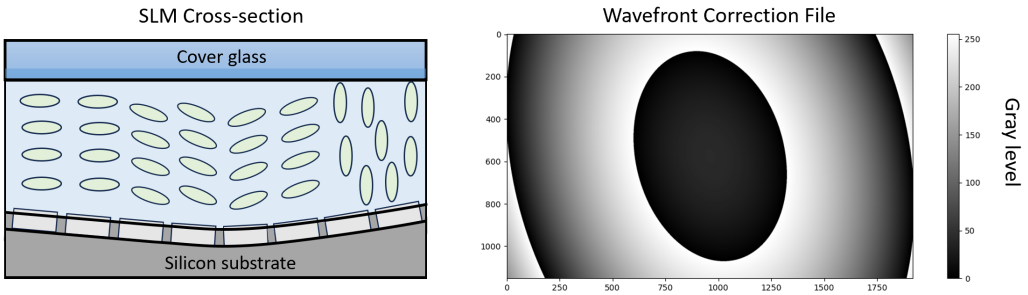

Figure 2. Wavefront correction file used to compensate for the SLM's intrinsic aberrations due to the manufacturing process, such as the curved silicon back panel.

3. SLM SOFTWARE CONTROL

Based on the Software Developer Kit (SDK) provided by the manufacturer, we developed a software package to interface and control the SLM. It allows to apply phase patterns on the SLM from a user defined image containing a wavefront expressed in terms of optical path difference. The package has been integrated into PLICO (Python Laboratory Instrumentation COntrol) [12]. This framework is designed to assist developers of instrument control applications, with a focus on interfacing with the most frequently utilized devices in adaptive optics laboratories. It was developed using the Python environment and is available on GitHub [13]. The manufacturer provides the BlinkOverDrivePlus software [10], referred to as Blink, to display phase patterns on the SLM. However, we find that Blink and PLICO do not give the same result for equivalent modes. We study the example of Zernike polynomials.

For instance, in Figure 3 and 4, we show the comparison of the phase patterns for the same astigmatism Z_6, with an amplitude $c_6 = 2\mu m$ rms. In both cases, there is no superposition of the WFC.

Figure 4 shows that these phase patters are slightly different inside the pupil. The phase pattern applied on the SLM is a result of a modulo 256 operation, whose profile is represented in magenta, that is then converted into 8-bit integers. The difference arise in the conversion to the 8-bit integer. While Blink (in blue) uses a floor division operation, PLICO (in red) uses a true rounding operation. As a result, our software gives us a better approximation of the expected phase pattern.

4. OPTICAL BENCH

Figure 5 shows the optical scheme of the test bench employed in the preliminary phase of this work. A 633 nm expanded laser beam illuminates a circular pupil stop of 10.5 mm diameter, placed in front of the SLM. The polarization of the incident beam is linear and aligned to the LC optical axis, along the y-axis. The incident beam is reflected by the SLM reflective pixel and imaged into the back focal plane of an objective lens L2, where a CCD camera is placed.

The angle α between the incoming and reflected beams is $\sim 6°$. The off-axis optical scheme is adopted to avoid using a beam splitter in an on-axis configuration. This increases the light throughput and reduces the number of optical surfaces that can introduce unwanted aberrations. In this case, a new calibration of the SLM is highly recommended as the angle of incidence could strongly affect the phase modulation. Indeed, the angle of incidence should be quasi normal in order to reduce cross-talk effects as the beam travels through more than one pixel region. However, if it is less then 10° there is no substantial modification in the modulation properties as the phase wrap value is still closer to the designed value [10][14].

Thus, in this preliminary phase of the work, we are controlling the SLM through the calibration provided by the manufacturer.

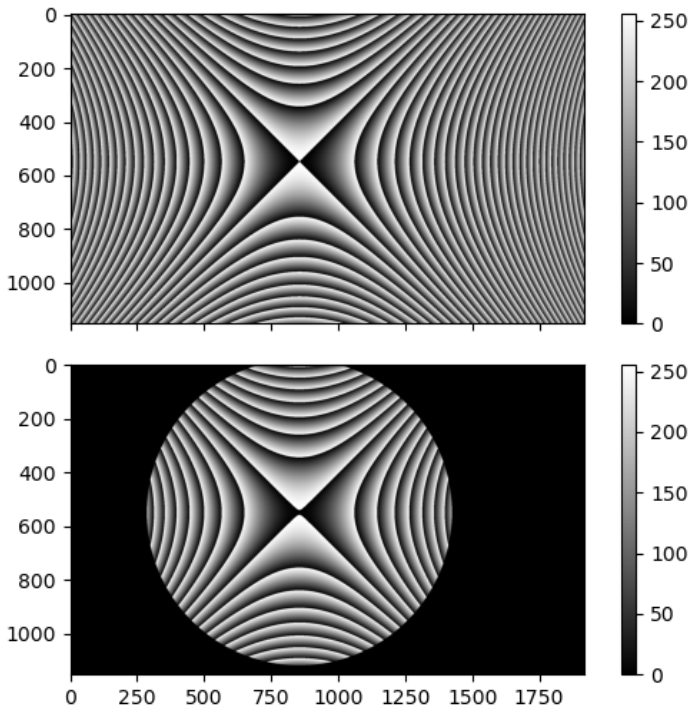

Figure 3. Phase pattern of the astigmatism $Z_6 = \sqrt{6}\rho^2 cos(2\theta)$ with amplitude $c_6 = 2\mu m$ rms reproduced with Blink (on top) and PLICO (bottom), without the superposition of the WFC. The Astigmatism is defined in a circular pupil with a radius R of 596 pixel and centred in (853, 550) pixel in a frame that represents the SLM display.

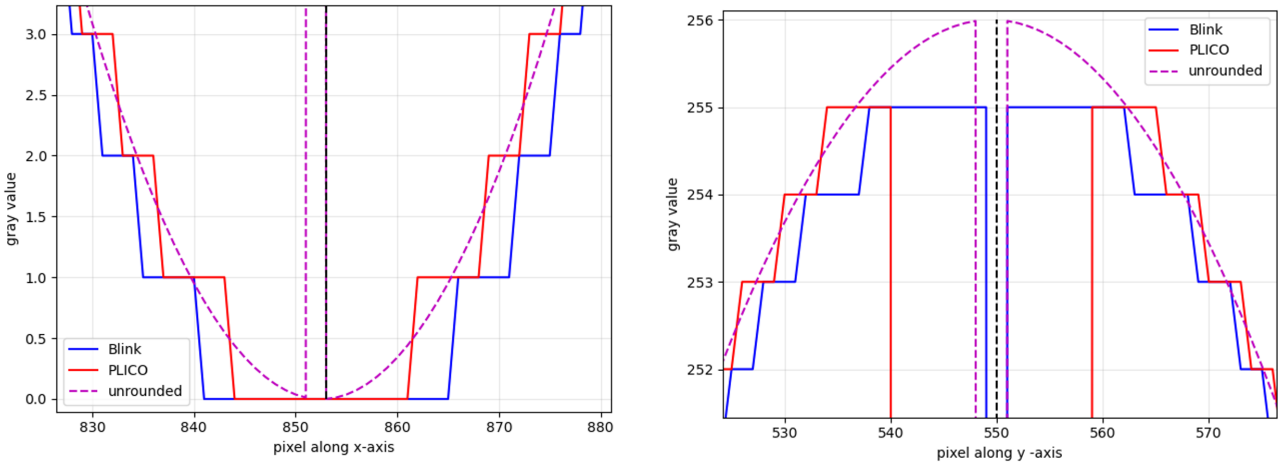

Figure 4. Phase pattern profile of the astigmatism $Z_6 = \sqrt{6}\rho^2 cos(2\theta)$ with amplitude $c_6 = 2\mu m$ rms, around the center of the circular pupil of (853, 550) pixel coordinates. The lines represent the phase pattern value assumed in each pixel. In magenta is shown the value of the phase pattern before the conversion into 8-bit integer value, while in blue and red are shown respectively the 8-bit integer phase pattern obtained with Blink and PLICO. Finally, the black dashed line represents the center coordinates of the circular pupil. We get a better approximation of the expected phase pattern through our software.

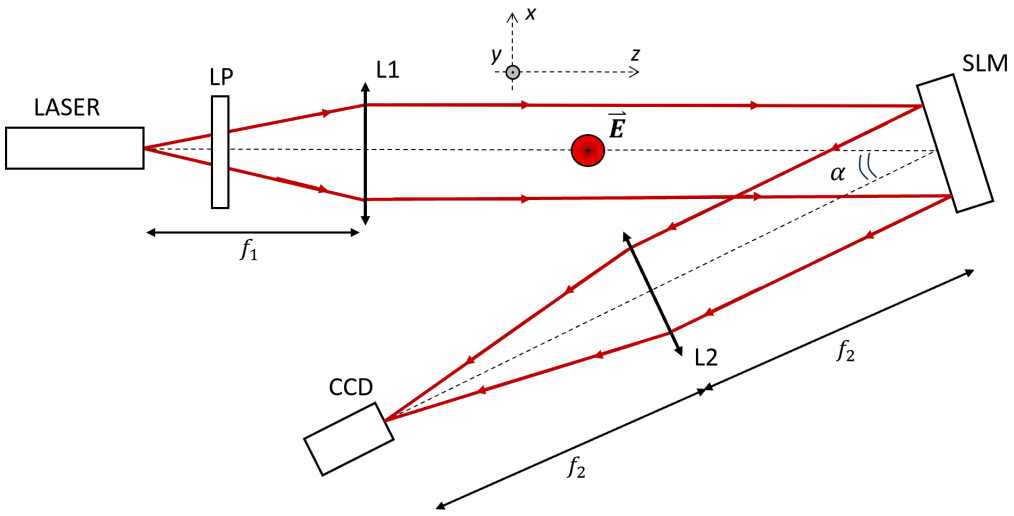

Figure 5. Optical scheme of the test-bench. A linearly polarized beam illuminates the SLM and is imagined to an objective lens where a CCD camera is place. The electric field $\vec{E}$ lies on the y axis and is parallel to the LC optical axis of the SLM. LP is a linear polarizer, L1 is the beam expander lens while L2 is the objective lens.

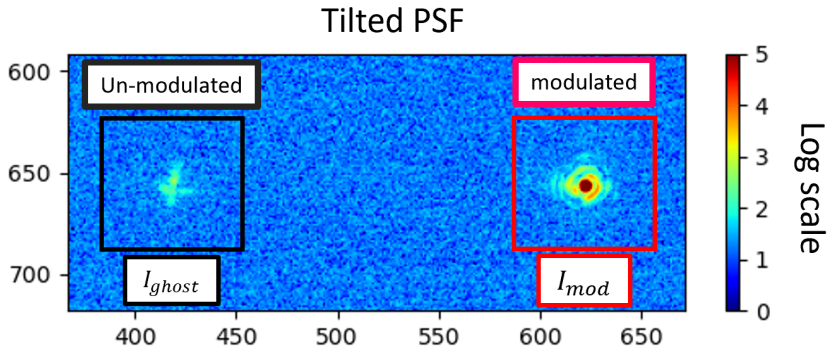

Figure 6. Region of interest after the application of a tilt on the SLM. The residual fraction of the reflected beam that lies in the zero order specular reflection corresponds to the non-modulated spot (I_{ghost}), while most of the light is tilted (I_{mod}).

5. ANALYSIS

5.1 Non-modulated zero-order spot

The SLM reflected beam is usually contaminated by a friction of light which prevents a full phase modulation. This results in a non-modulated spot in the specular reflection, often referred to as a zero-order spot or ghost. Several factors can contribute to this spot, such as misalignment between the incident polarisation and the SLM LC optical axis, deploarisation effects due LC molecules fluctuations, the intrinsic pixellated structure of such devices, among the others. [11, 14, 15, 16, 17, 18, 19]

To characterize the magnitude of the zero order spot, we display a tilt, $Z_2 = 2\rho cos(\theta)$, on the SLM and measure the intensity in the regions relative to the ghost, I_{ghost}, and the tilted spot, I_{mod}, as show in Figure 6. Both intensities are normalized to one, I_{flat}, measured in the ghost region when the flat command is displayed on the SLM.

Figure 7 shows the normalized intensities acquired by applying a tilt of 4 μm rms as a function of the rotation angle of the linear polariser. A fine tuning around the optimised rotation angle resulted in I_{mod}/I_{flat}= (96 $\pm$ 5)% and I_{ghost}/I_{flat} = (5 $\pm$ 2)% for the tilted and ghost spots, respectively.

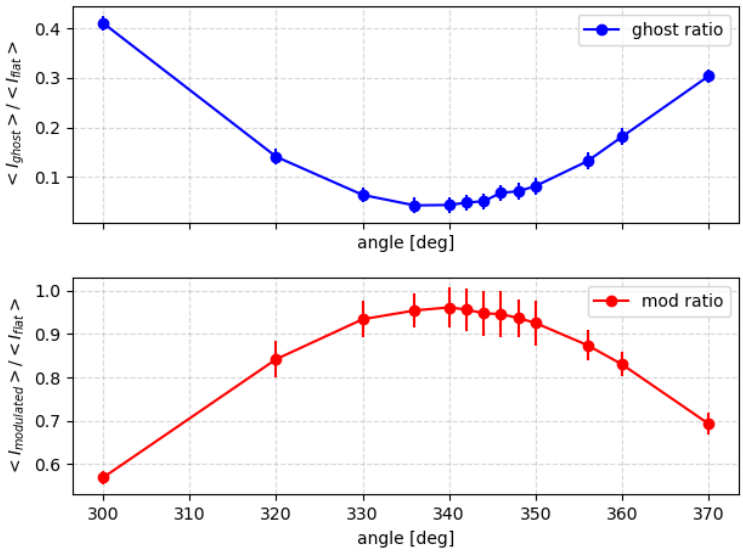

Figure 7. Intensity ratios as a function of the rotation angle of the linear polarizer. The intensity ratio measured in the ghost and tilted region of interest are shown in blue and red, respectively.

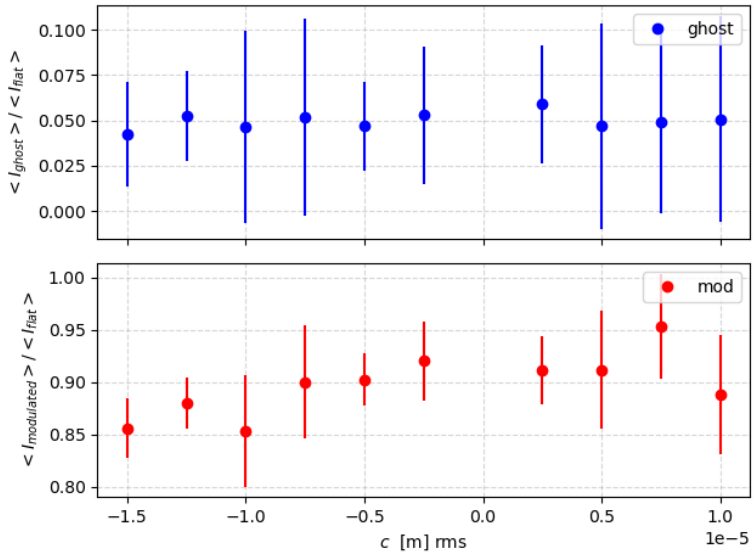

Figure 8. Intensity ratios as a function of the amplitude c rms of the applied tilt, $Z_2 = 2\rho cos(\theta)$. The measured values in the ghost and tilted region of interest are shown in blue and red, respectively. The ghost is constant while for $|c| \geq 10\mu$m rms we observe a loss in the modulable spot.

Depolarisation effects and any deviation from pure linear phase modulation with 2π modulation depth can result in a loss of diffraction efficiency [18, 19]. In Figure 8, we measure the normalized ghost and tilted spot intensities as a function of the applied tilt coefficient c. We observe a constant ratio for the ghost spot ($I_{ghost}/I_{flat} \simeq 5\%$) and a loss of $\leq 10\%$ in the total intensity ($I_{tot} = I_{ghost}/I_{flat} + I_{mod}/I_{flat}$) for tilt coefficients $|c| \geq 10\mu$m rms. Further studies are required to understand the loss in the total reflected intensity, I_{tot}.

5.2 PSF Sharpening

To reduce system aberrations we are currently using a sensorless AO scheme, by individually adjusting the first Zernike polynomials on the SLM.

Zernike modes from (Z_4 to Z_{11}) has been display on a circular pupil mask of 571 pixel with amplitude c_j values in the range of $\pm$200 nm rms. Following [20], as image quality parameter, hereafter refereed as merit value, has been chosen the image standard deviation of the pixel in a region of 50x50 pixel centred on the measured PSF.

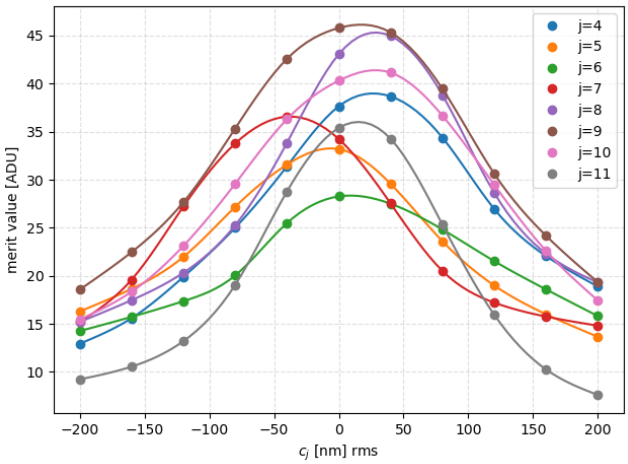

Figure 9. Measured image standard deviation (merit value) as a function of the amplitude c_j of each displayed Zernike mode on the SLM. The dots represents the measurements while the solid lines are the cubic spline interpolated function.

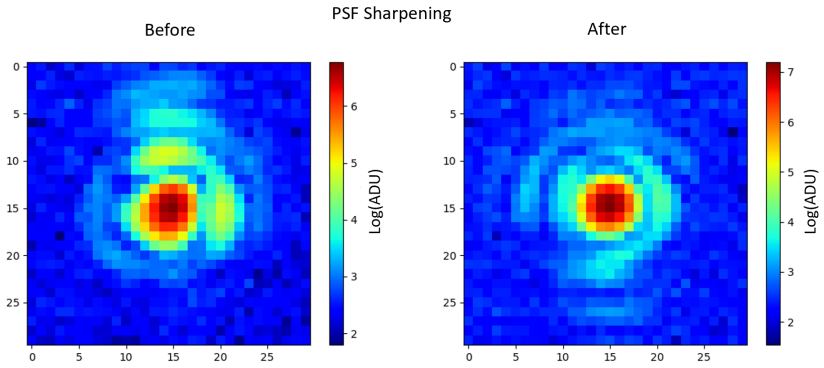

Figure 10. PSF image before and after the compensation of system aberration. Before the sharpening, only the SLM was set to the flat command.

Referring to Figure 9, the compensation of system aberration is obtained through a Cubic spline interpolation of the measured merit values for each displayed mode. Thus, the amplitudes to remove system aberration are estimated as those values corresponding to the maximum of the interpolated curves.

This scheme has been applied once the SLM is set the flat command, namely when only the WFC is displayed on the SLM, and then loading a tilt of amplitude $c_2 = -10\mu$m rms, in order to spatially separate the tilted PSF from the un-modulable ghost.

In Figure 11 and Table 1 are reported the estimated Zernike coefficient. In Table 2 are reported the peak and the FWHM of the measured PSF before and after the system aberration compensation. These values has been estimated through a Gaussian fit on the measured PSF. An example is shown in Figure 10. The expected FWHM in diffraction limit is 3.3 pixel ($\sim$15μm).

5.3 Tip/Tilt response

To test the linear response of the SLM we compute the displacement of the PSF centroid along the image plane axis, due the application of a tip/tilt on the SLM.

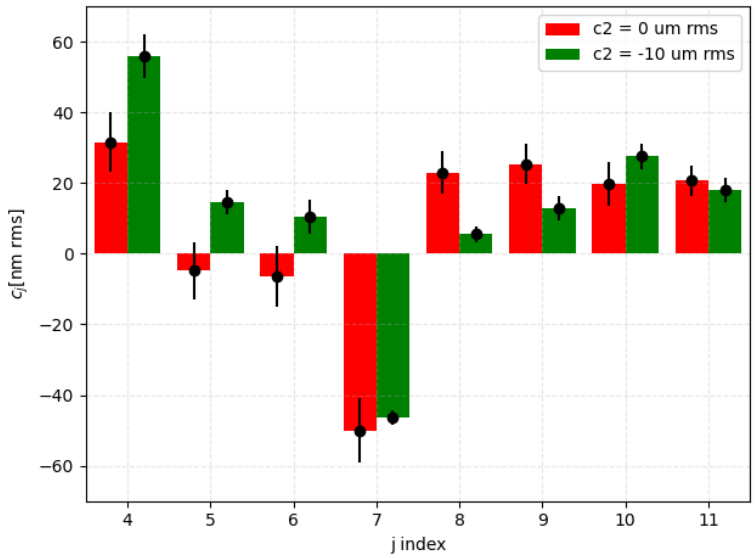

Figure 11. Zernike coefficient obtained from the sensorless AO scheme to compensate system aberration. The red bars are those estimated from the PSF obtained when the SLM is set to flat, while the green ones are those estimated when a tilt of amplitude -10μm rms is applied.

Table 1. Estimated parameter for system aberration compensation in the case of applying a tilt of -10μm rms and the flat command on the SLM.

	[nm rms]							
	c_4	c_5	c_6	c_7	c_8	c_9	c_{10}	c_{11}
Tilt	51 ± 6	15 ± 4	10 ± 5	-46 ± 2	6 ± 2	13 ± 3	28 ± 4	18 ± 4
Flat	32 ± 8	-5 ± 8	-6 ± 9	-50 ± 9	23 ± 6	25 ± 6	20 ± 6	21 ± 4

The expected displacement Δ_{exp} of the PSF is calculated as follows:

$$\Delta_{exp} \simeq f \, \frac{4\,c}{D} \tag{2}$$

where f is the focal length of the objective lens, D is the diameter of the pupil stop and c is the rms amplitude for the displayed tip/tilt. The displacement is measured from a Gaussian fit on the tip/tilted PSF and are reported in Figure 12.

From the linear regression, the R^2 has been compute as follows:

$$R^2 = \frac{\Sigma(\Delta_{fit} - \Delta_{exp})^2}{\Sigma(\Delta_{meas} - \Delta_{exp})^2} \tag{3}$$

where Δ_{meas} is the measured displacement and Δ_{fit} is the one inferred from the linear fit. From the data we observed a $R^2_{Z_2} = 99.87\%$ and $R^2_{Z_3} = 96.47\%$ when applying tip/tilt.

Estimates of R^2 show that the SLM has a linear response with a relative error of ≤ 2 % on the measured displacement.

6. FUTURE TASKS

The next step, is to characterize the SLM through a WFS. A SH-WFS will be included on the optical bench, as show in Figure 13, to sense the wavefront aberrations. The SLM will be used to inject and also compensate aberrations, whose correction performance will be analyzed through the PSF. Particularly, to simulate MORFEO's wide field, the projection of the atmospheric turbulent volume along the line of sight of each of the 12 WFSs foreseen for MORFEO will be computed then displayed on the SLM to be sensed through the SH-WFS. The

Table 2. Parameters derived from the Gaussian fit on the PSF after and before system aberration compensation in the case of applying a tilt of -10μm rms and the flat command on the SLM.

	Compensation	Amplitude [ADU]	$FWHM_x$ [pixel]	$FWHM_y$ [pixel]
Tilt	before	780 ± 60	4.2 ± 0.3	3.9 ± 0.3
	after	1420 ± 90	3.4 ± 0.1	3.3 ± 0.1
Flat	before	880 ± 70	3.5 ± 0.3	4.0 ± 0.3
	after	1420 ± 40	3.5 ± 0.1	3.3 ± 0.1

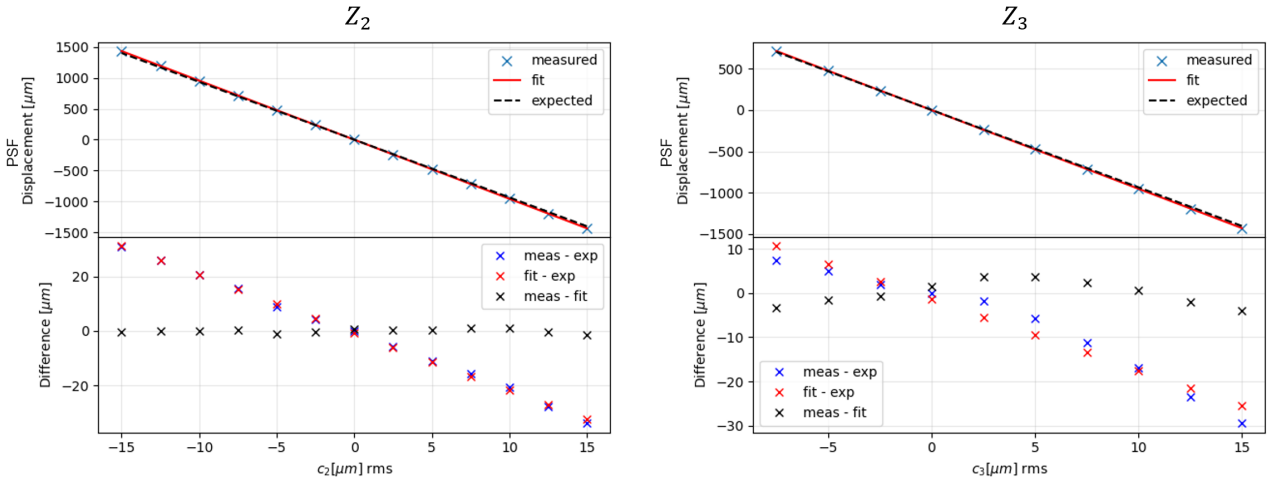

Figure 12. PSF displacement along the x-axis (left) and y-axis (right) as a function of the applied amplitude for Z_2 and Z_3, respectively. In the upper panels, the crosses represent the measured displacement, the red solid line represents the linear fit and the black dashed line is the expected displacement. The lower panels show the displacements difference between the measured and expected (in blue), the fitted and expected (in red) and the measured and fitted (in black).

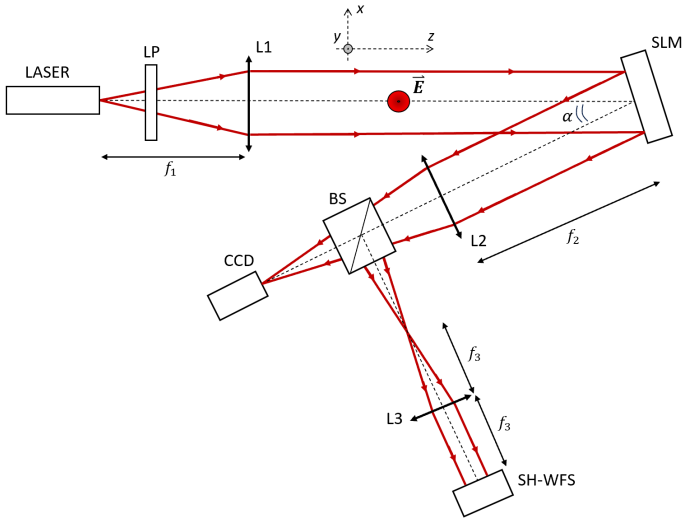

Figure 13. Optical scheme of SCAO test bench. To sense wavefront aberration a SH-WFS is included in the current optical bench, shown in Figure 5, with a the lens L3 to reimage the SLM on the WFS, and with a beam splitter BS to analyze the correction performance through the PSF.

measurements from all the WFS will be used to compute the tomographic reconstructor and to infer the commands to the SLM.

Finally, the whole process will be reiterated by shifting the simulated phase maps, in order to take into account the temporal evolution effects between successive iterations of the control loop.

We will analyse and test the reconstruction and control algorithms foreseen for MORFEO through a simplified SCAO system test-bed and a numerical simulator.

7. CONCLUSION

MORFEO shows new and challenging issues, that need to be tested and prototyped. To do so, we aim at analyzing and testing the reconstruction and control algorithms foreseen for MORFEO on a simplified single-conjugated adaptive optics system test-bed and a numerical simulator. To inject and also compensate for the disturbances, we are using a 1920x1152 XY Phase Series Spatial Light Modulator manufactured by Meadowlark Optics. In this context, as a first step of our project we want to characterize it.

In this preliminary work, we developed software tools based on the manufacturer SDK that allow us to control and interface the SLM in the Python environment. These packages has been integrated into PLICO.

We observed and try to mitigate the non-modulated spot in the specular reflection of the SLM (often known as zero order spot) by adjusting the orientation of the linear polarizer with respect to the LC optical axis, and analysing the intensity of this spot as a function of the applied tilt on the SLM. The results shows that the intensity of the ghost spot is in the order of 5% of the total reflected intensity.

Adopting a sensorless AO scheme, we are able to compensate the main system aberration up to spherical aberration Z_{11}. Through this scheme we measured a PSF with a FWHM close to the diffraction limit.

We observed that the SLM has a linear response to the displayed tip/tilt. The results show that the measured PSF centroid displacements along the axis of CCD plane has a relative error $\leq 2\%$.

The next step, is to include a Shack-Hartmann Wavefront Sensor (SH-WFS) in the optical bench, to sense the wavefront aberrations. The SLM will be used to inject and also compensate aberrations, whose correction performance will be analyzed through the PSF.

References

[1] Paolo Ciliegi et al. "MAORY: the adaptive optics module for the Extremely Large Telescope (ELT)". In: *Adaptive Optics Systems VII*. Ed. by Laura Schreiber, Dirk Schmidt, and Elise Vernet. Vol. 11448. Society of Photo-Optical Instrumentation Engineers (SPIE) Conference Series. Dec. 2020, 114480Y, 114480Y. DOI: 10.1117/12.2561754.

[2] Roberto Tamai et al. "The ESO's ELT construction progress". In: *Ground-based and Airborne Telescopes VIII*. Ed. by Heather K. Marshall, Jason Spyromilio, and Tomonori Usuda. Vol. 11445. Society of Photo-Optical Instrumentation Engineers (SPIE) Conference Series. Dec. 2020, 114451E, 114451E. DOI: 10.1117/12.2562828.

[3] Yann Clénet et al. "The MICADO first light imager for the ELT: overview of the SCAO module at its final design". In: *Adaptive Optics Systems VIII*. Ed. by Laura Schreiber, Dirk Schmidt, and Elise Vernet. Vol. 12185. Society of Photo-Optical Instrumentation Engineers (SPIE) Conference Series. Aug. 2022, 121854S, 121854S. DOI: 10.1117/12.2629856.

[4] L. Busoni. "MORFEO enters final design phase". In: These proceedings.

[5] Thierry Fusco et al. "Multiconjugate adaptive optics: comparison of phase reconstruction approaches for large field of view". In: *Atmospheric Propagation, Adaptive Systems, and Laser Radar Technology for Remote Sensing*. Ed. by John D. Gonglewski et al. Vol. 4167. International Society for Optics and Photonics. SPIE, 2001, pp. 168–179. DOI: 10.1117/12.413820. URL: https://doi.org/10.1117/12.413820.

[6] Thierry Fusco et al. "Optimal wave-front reconstruction strategies for multiconjugate adaptive optics". In: *Journal of the Optical Society of America A* 18.10 (Oct. 2001), pp. 2527–2538. DOI: 10.1364/JOSAA.18.002527.

[7] Brent L. Ellerbroek and Curtis R. Vogel. "Simulations of closed-loop wavefront reconstruction for multiconjugate adaptive optics on giant telescopes". In: *Astronomical Adaptive Optics Systems and Applications*. Ed. by Robert K. Tyson and Michael Lloyd-Hart. Vol. 5169. Society of Photo-Optical Instrumentation Engineers (SPIE) Conference Series. Dec. 2003, pp. 206–217. DOI: 10.1117/12.506580.

[8] Avinash Surendran et al. "Daytime calibration and testing of the Keck All sky Precision Adaptive optics tomography system". In: *Adaptive Optics Systems VIII*. Ed. by Laura Schreiber, Dirk Schmidt, and Elise Vernet. Vol. 12185. Society of Photo-Optical Instrumentation Engineers (SPIE) Conference Series. Aug. 2022, 121851V, p. 121851V. DOI: 10.1117/12.2628264. arXiv: 2207.14433 [astro-ph.IM].

[9] Zichen Zhang, Zheng You, and Daping Chu. "Fundamentals of phase-only liquid crystal on silicon (LCOS) devices". In: *Light: Science and Applications* 3 (Oct. 2014). DOI: 10.1038/lsa.2014.94.

[10] Meadowlark Optics. *User Manual XY Phase Series Spatial Light Modulatos With PCIe Controller*. Version Rev. 1.07. Meadowlark Optics, Inc. 52 pp.

[11] A. A Pushkina et al. "Comprehensive model and performance optimization of phase-only spatial light modulators". In: *Measurement Science and Technology* 31.12, 125202 (Dec. 2020), p. 125202. DOI: 10.1088/1361-6501/aba56b. arXiv: 2005.01561 [physics.optics].

[12] C. Selmi et al. "PLICO: a framework for Adaptive Optics laboratory experiments". In: These proceedings.

[13] *PLICO Repository on GitHub*. https://github.com/ArcetriAdaptiveOptics/plico.

[14] A. Lizana et al. "Influence of the incident angle in the performance of Liquid Crystal on Silicon displays". In: *Optics Express* 17.10 (May 2009), p. 8491. DOI: 10.1364/OE.17.008491.

[15] A. Márquez et al. "Mueller-Stokes characterization and optimization of a liquid crystal on silicon display showing depolarization". In: *Optics Express* 16.3 (Jan. 2008), p. 1669. DOI: 10.1364/OE.16.001669.

[16] Angel Lizana et al. "Time-resolved Mueller matrix analysis of a liquid crystal on silicon display". In: 47.23 (Aug. 2008), p. 4267. DOI: 10.1364/AO.47.004267.

[17] Justin E. Wolfe and Russell A. Chipman. "Polarimetric characterization of liquid-crystal-on-silicon panels". In: 45.8 (Mar. 2006), pp. 1688–1703. DOI: 10.1364/AO.45.001688.

[18] Ignacio Moreno et al. "Diffraction efficiency of stepped gratings using high phase-modulation spatial light modulators". In: *Optics and Lasers in Engineering* 126, 105910 (Mar. 2020), p. 105910. DOI: 10.1016/j.optlaseng.2019.105910.

[19] A. Lizana et al. "Time fluctuations of the phase modulation in a liquid crystal on silicon display: characterization and effects in diffractive optics". In: *Opt. Express* 16.21 (Oct. 2008), pp. 16711–16722. DOI: 10.1364/OE.16.016711. URL: https://opg.optica.org/oe/abstract.cfm?URI=oe-16-21-16711.

[20] A. Barbotin. *Alignment of an SLM-based STED depletion beam*. Feb. 2020. DOI: 10.5281/zenodo.3567748. URL: https://doi.org/10.5281/zenodo.3567748.